

Post-process correction improves the accuracy of satellite PM_{2.5} retrievals

Andrea Porcheddu¹, Ville Kolehmainen¹, Timo Lähivaara¹, and Antti Lipponen²

¹Department of Technical Physics, University of Eastern Finland, Kuopio, Finland

²Finnish Meteorological Institute, Atmospheric Research Centre of Eastern Finland, Kuopio, Finland

Correspondence: Andrea Porcheddu (andrea.porcheddu@uef.fi)

Abstract. Estimates of PM_{2.5} levels are crucial for monitoring air quality and studying the epidemiological impact of air quality on the population. Currently, the most precise measurements of PM_{2.5} are obtained from ground stations, resulting in limited spatial coverage. In this study, we consider satellite-based PM_{2.5} retrieval, which involves conversion of high-resolution satellite retrieval of Aerosol Optical Depth (AOD) into high-resolution PM_{2.5} retrieval. To improve the accuracy of the AOD to PM_{2.5} conversion, we employ the machine learning based post-process correction to correct the AOD-to-PM conversion ratio derived from Modern-Era Retrospective analysis for Research and Applications, Version 2 (MERRA-2) reanalysis model data. The post-process correction approach utilizes a fusion and downscaling of satellite observation and retrieval data, MERRA-2 reanalysis data, various high resolution geographical indicators, meteorological data and ground station observations for learning a predictor for the approximation error in the AOD to PM_{2.5} conversion ratio. The corrected conversion ratio is then applied to estimate PM_{2.5} levels given the high-resolution satellite AOD retrieval data derived from Sentinel-3 observations. The region of study is central Europe during the year 2019. Our model produces PM_{2.5} estimates with a spatial resolution of 100 meters at satellite overpass times with $R^2 = 0.55$ and RMSE = $6.2 \mu\text{g}/\text{m}^3$. The corresponding metrics for monthly averages are $R^2 = 0.72$ and RMSE = $3.7 \mu\text{g}/\text{m}^3$. Additionally, we have incorporated an ensemble of neural networks to provide error envelopes for machine learning related uncertainty in the PM_{2.5} estimates. The proposed approach can produce accurate high resolution PM_{2.5} data that can be very useful for air quality monitoring, emission regulation and epidemiological studies.

1 Introduction

Poor air quality is one of the most serious environmental health risks of our time. In September 2021, the World Health Organization (WHO) released Global Air Quality Guidelines, revealing clear evidence of the damage air pollution inflicts on human health at even lower concentrations than previously understood (World Health Organization, 2021). WHO estimates that exposure to air pollution causes 7 million premature deaths every year. A key indicator in monitoring air quality and epidemiological studies is the PM_{2.5} parameter, which is the dry mass concentration of fine particulate matter with an aerodynamic diameter of less than 2.5 micrometers (micrograms of particulate matter per cubic meter of air). Fine particulate matter originates from vehicle emissions, coal burning, and industrial emissions, among many other human and natural sources. Epidemiological studies link long exposures to high PM_{2.5} levels to many severe illnesses, such as stroke and cardiovascular and respiratory

25 diseases (e.g. Pope and Dockery, 2006; Cohen et al., 2017). On a global scale, the magnitude of the PM_{2.5} exposure-related risk for human health is enormous as more than 90% of the world's population lives in areas with annual mean PM_{2.5} levels exceeding the new WHO 2021 air quality guideline of 5 micrograms per cubic meter (Health Effects Institute, 2019).

While the knowledge of the health effects of pollution increases continuously, the epidemiological estimates still have significant uncertainties due to the lack of accurate global air pollution data (Hammer et al., 2020). Networks of ground-based
30 observation stations produce accurate pointwise observations of PM_{2.5} and certain chemical components such as ozone, sulfur dioxide and nitrogen dioxide. These ground station measurements produce relatively accurate data, but the networks consist of only a few thousand irregularly located observation stations, mainly in developed countries, leading to the insufficient spatial coverage of the PM_{2.5} data. To better monitor and understand air quality and pollution sources near real-time global observations of air quality are needed. The only way to get spatially resolved air quality data is to utilize satellite retrievals.

35 Satellite retrievals of PM_{2.5} are often based on satellite AOD retrievals and [an](#) AOD-to-PM conversion ratio (Health Effects Institute, 2019; van Donkelaar et al., 2013; Zhang and Kondragunta, 2021; Geng et al., 2015). AOD is a columnar optical quantity, whereas PM_{2.5} is the mass concentration of dry aerosol particles at some single point, typically at the surface level. Many factors affect the AOD-to-PM conversion ratio, including the aerosol vertical extinction profile, aerosol type and size distribution, and relative humidity. These factors are typically unavailable from a single data source, such as data provided by
40 the instruments onboard a satellite, so a simulation-model-based AOD-to-PM ratio is often used. The simulation-model-based AOD-to-PM conversion ratio is typically computed based on meteorology, chemical transport models (CTM) and auxiliary satellite data such as lidar-based aerosol vertical profiles. The PM_{2.5} retrieval at a given location and time is then calculated as a product of the retrieved satellite AOD and the AOD to PM_{2.5} ratio. The current state-of-the-art PM_{2.5} retrieval algorithm also contains a post-processing step where the retrieved spatial PM_{2.5} estimate is fitted to the ground-based PM_{2.5} station data
45 by a linear geographically weighted regression (van Donkelaar et al., 2016).

[Many previous studies use machine learning techniques to convert AOD to PM_{2.5} levels. In particular, \(Ibrahim et al., 2022\) used a variant of Random Forest called Extremely Randomised Trees \(ET\) to estimate PM_{2.5} across Europe. \(Stafoggia et al., 2019; Schneid](#)
[used Random Forest regressors in a multi-stage approach to estimate PM_{2.5} at ground stations when only PM₁₀ measurements were available, to impute AOD values when not accessible and to finally predict PM_{2.5} values across Italy and Great Britain.](#)
50 [\(Handschuh et al., 2023\) considered multiple Random Forest models to evaluate PM_{2.5} levels across Germany using 4 different AOD datasets.](#)

In this paper, we propose a novel approach for high-resolution satellite-based retrieval of PM_{2.5}. [While the previous studies use machine learning to learn the AOD to PM_{2.5} conversion directly, we take a novel approach where we train the model to predict the approximation error in the geophysical model based conversion ratio.](#) Our approach retrieves PM_{2.5} at **the a**
55 spatial resolution of 100 m. It is based on the machine learning post-process correction approach, which we developed for the correction of approximation errors in satellite retrievals (Lipponen et al., 2021) and employed for high-resolution spectral aerosol optical depth (AOD) retrieval (POPCORN AOD) from SENTINEL-3 SYNERGY data (Lipponen et al., 2022). In our algorithm development work, we take the spectral, high-resolution Sentinel-3 POPCORN AOD (Lipponen et al., 2022) as the starting point. Our PM_{2.5} retrieval is based on the AOD-to-PM_{2.5} conversion ratio applied to the POPCORN AOD. The

60 AOD-to-PM_{2.5} ratio is estimated by machine learning techniques utilizing a fusion of collocated ground station-based in-situ
PM_{2.5} data, MERRA-2 reanalysis model AOD and PM_{2.5} data, spectral AERONET AOD, satellite-observed spectral top-
of-atmosphere reflectances, meteorology data and various high-resolution geographical indicators representing, for example,
population density and land surface elevation. Utilizing these data, we employ the post-process correction approach to the
estimation of [the](#) AOD-to-PM_{2.5} ratio (Lipponen et al., 2021, 2022; Taskinen et al., 2022) and then the high-resolution PM_{2.5}
65 retrieval is obtained as the product of the post-process corrected AOD-to-PM_{2.5} ratio and POPCORN AOD. By using an
ensemble of neural networks, we can also provide error envelopes for the machine learning related uncertainty in the PM_{2.5}
estimates. The approach is tested with Sentinel-3 data from central Europe in 2019.

2 Data

We use various input data variables in computing the estimate for the surface PM_{2.5}. We use satellite observation data and
70 retrievals, in-situ observations, and reanalysis model data. This section lists all the variables and data sources used in our work.

2.1 Sentinel-3 POPCORN AOD

[The](#) Sentinel-3 POPCORN AOD product is based on [the](#) post-process corrected Sentinel-3 SYNERGY land AOD product. It
offers a spatial resolution of 300 meters and is currently accessible for Sentinel-3A and 3B overpasses, covering five regions of
interest for the year 2019: Central Europe, Eastern USA, Western USA, Southern Africa, and India. [Two Sentinel-3 satellites](#)
75 [currently flying provide revisit times of less than two days for OLCI and less than one day for the SLSTR instrument at equator.](#)
[Swath width of the OLCI instrument is 1270 km. SLSTR swath width is 1420 km for the nadir view and 750 km for the oblique](#)
[view.](#)

The post-process correction is based on a feed forward neural network that was trained to predict the bias in Sentinel-3
Synergy AOD. Sentinel-3-AERONET-collocated data was used as the training data for the neural network and the trained
80 neural network was then used for bias correction and superresolution of the Sentinel-3 AOD (land) data. The idea for post-
process correction of satellite AOD retrievals was introduced in Lipponen et al. (2021). For the technical details and accuracy
metrics of Sentinel-3 SYNERGY land POPCORN AOD, and related openly available code and data, see Lipponen et al. (2022).

In this work, we use POPCORN AODs at 440, 500, 550, 675, and 870 nm, and the Angstrom exponent derived using
AODs at these wavelengths as inputs for the AOD-to-PM_{2.5} ratio model. POPCORN AODs are the data that bring the accurate
85 AERONET AOD information to the AOD-to-PM_{2.5} conversion.

2.2 OpenAQ

OpenAQ (<https://openaq.org/>) is an open database for air quality data. In this work, we use OpenAQ as our data source for
surface in-situ PM_{2.5} observations. OpenAQ provides pointwise air quality measurement data for thousands of stations. The
temporal resolution of the data provided varies by station, 1-hour and daily observations are commonly available. See Figure 1
90 for a map of OpenAQ stations providing hourly data in our region of interest.

Some OpenAQ stations report 24 hour average $PM_{2.5}$ every hour.

In this work, we used the 24 hour averages given every hour to estimate hourly $PM_{2.5}$. This was done station-by-station using a Tikhonov regularized (with regularization parameter value 0.05) least-squares fit to unfold the time integrated data into hourly estimates.

95 In practice, the hourly $PM_{2.5}$ estimates were computed using the formula

$$\underline{PM_{2.5,1h}} = (A^T A + \alpha I)^{-1} A^T b, \quad (1)$$

where

$$A = \begin{bmatrix} \frac{1}{24} & \frac{1}{24} & \cdots & \frac{1}{24} & 0 & 0 & \cdots & 0 \\ 0 & \frac{1}{24} & \cdots & \frac{1}{24} & \frac{1}{24} & 0 & \cdots & 0 \\ & & & \vdots & & & & \\ 0 & 0 & \cdots & 0 & 0 & 0 & \cdots & \frac{1}{24} \end{bmatrix}, \quad (2)$$

$$100 \quad b = \begin{bmatrix} PM_{2.5,24h,1} \\ PM_{2.5,24h,2} \\ \vdots \\ PM_{2.5,24h,N} \end{bmatrix}, \quad (3)$$

$$\underline{PM_{2.5,1h}} = \begin{bmatrix} PM_{2.5,1h,24} \\ PM_{2.5,1h,25} \\ \vdots \\ PM_{2.5,1h,N} \end{bmatrix}, \quad (4)$$

and α is the regularization parameter. $PM_{2.5,1h,N}$ and $PM_{2.5,24h,N}$ denote the 1 hour and 24 hour average $PM_{2.5}$ at timestep N , respectively.

105 2.3 MERRA-2

The Modern-Era Retrospective analysis for Research and Applications, Version 2 (MERRA-2) is NASA's reanalysis model (Randles et al., 2017). MERRA-2 provides us meteorological variables, such as wind fields and temperatures. Furthermore, MERRA-2 reanalysis also has the necessary aerosol and air quality information to compute an estimate for the surface $PM_{2.5}$.

MERRA-2 has a spatial resolution of $0.5^\circ \times 0.625^\circ$. This is roughly 50 km in Central Europe region. The time-varying
110 MERRA-2 variables we use have the temporal resolution of 1 hour and both instantaneous values or time-averaged values are

given depending on the variable and data product. We also use some MERRA-2 constant variables as inputs for our AOD-to-PM_{2.5} model. See the Appendix A for a list of all variables we have used as inputs in our models from the MERRA-2 re-analysis.

115 In addition to MERRA-2 provided variables, the following variables are derived using the MERRA-2 meteorology and aerosol-related variables and used in our models as inputs:

- **Relative humidity (RH) at the surface.** [Equation based on the Clausius-Clapeyron equation \(see e.g. Michaelides et al., 2019\)](#)

:

$$RH = 0.263 \cdot PS \cdot QLML / \exp((17.67 \cdot (T2M - 273.15)) / (T2M - 29.65))$$

- **Wind direction (WD10M) at 10 meters:**

120 $WD10M = \arctan(-V10M/U10M)$

- **Wind speed (WS10M) at 10 meters:**

$$WS10M = \sqrt{U10M^2 + V10M^2}$$

- **PM_{2.5} at surface:** (Buchard et al. (2016))

$$PM_{2.5} = (1.375 \cdot SO4SMASS + 1.4 \cdot OCSMASS + BCSMASS + DUSMASS25 + SSSMASS25) \cdot 10^9$$

- 125 – **AOD-to-PM_{2.5} ratio η :**

$$\eta = \frac{PM_{2.5}}{TOTEXTTAU}$$

2.4 CALIOP aerosol vertical profile climatology

We use the Cloud-Aerosol Lidar and Infrared Pathfinder Satellite Observation (CALIPSO) Lidar Level-3 Tropospheric Aerosol Profiles, Cloud Free Data, Standard Version 4-20 data product as one of our input data source (NASA, 2022; Winker et al., 130 2010). This level-3 climatology data product has spatial resolution of 2.5 deg x 2 deg and temporal resolution of 1 month. We use daytime variables and in the case of missing data, we use the nearest value found in the dataset. We use two variables from this dataset: AOD 63 Percent Below and AOD 90 Percent Below. These variables indicate the vertical height below which 63 and 90 percent of AOD is located on average. This gives us information about the vertical distribution of aerosols in the atmosphere.

135 **2.5 Time variables**

Information about the time of day and year are given as inputs for the model. Both the yearly and daily fractions from the beginning of the year and day until the end of year and day, respectively, are mapped to a unit circle and the x and y coordinates of the unit circle points are used as inputs for the model. With this approach, we get very similar values for the end and beginning of the year and day.

140 2.6 High-resolution geographical indicators

2.6.1 OpenStreetMap roads

OpenStreetMap is an open map project and it contains map data with high spatial resolution. We use OpenStreetMap roads as a data source for our model inputs. We compute the distance to the nearest street or highway and use this distance as an input. [We use a 100 meter resolution grid for the distances.](#) The paths, streets and highways are all classified as 'highways' in
145 OpenStreetMap and we use only the following sub-classes to only accept roads and highways with car traffic and thus potential PM_{2.5} sources (information from (OpenStreetMap, 2023)). See Appendix A for all the OpenStreetMap road types used to compute the distance to the closest road.

2.6.2 NASA Black Marble Night Lights

NASA's Black Marble is a night light product based on Visible Infrared Imaging Radiometer Suite (VIIRS) day/night band
150 (DNB) radiances measured at nighttime. DNB is highly sensitive to light and can therefore detect even very low intensity lights on Earth surface at night. Most of the nighttime lights seen on Earth's surface are due to human activities. As human footprint is well seen in the night lights, we use the NASA Black Marble Night Lights as a proxy variable for the population density and use it as one input for our models. [We use Night Light data at spatial resolution of 500 meter as our input based on the yearly data product VNP46A4 \(Wang et al., 2020\).](#)

155 2.6.3 MODIS land cover type

We use MODIS MCD12Q1 (Sulla-Menashe and Friedl, 2018) land cover type data product to derive input variables that contain distances to the closest International Geosphere Biosphere Programme (IGBP) land cover types (Loveland and Belward, 1997; Belward et al., 1999). The spatial resolution of the MODIS MCD12Q1 data product is 500 meters. For the list of IGBP land cover types, see Appendix A.

160 2.6.4 Digital Elevation Model

We use the Advanced Spaceborne Thermal Emission and Reflection Radiometer (ASTER) digital elevation model (DEM) to describe the land surface elevation (Fujisada et al., 2011, 2012; NASA/METI/AIST/Japan Spacesystems, and US/Japan ASTER Science Team, 2019). ASTER DEM has a spatial resolution of 1 arcsecond corresponding to about 30 meters.

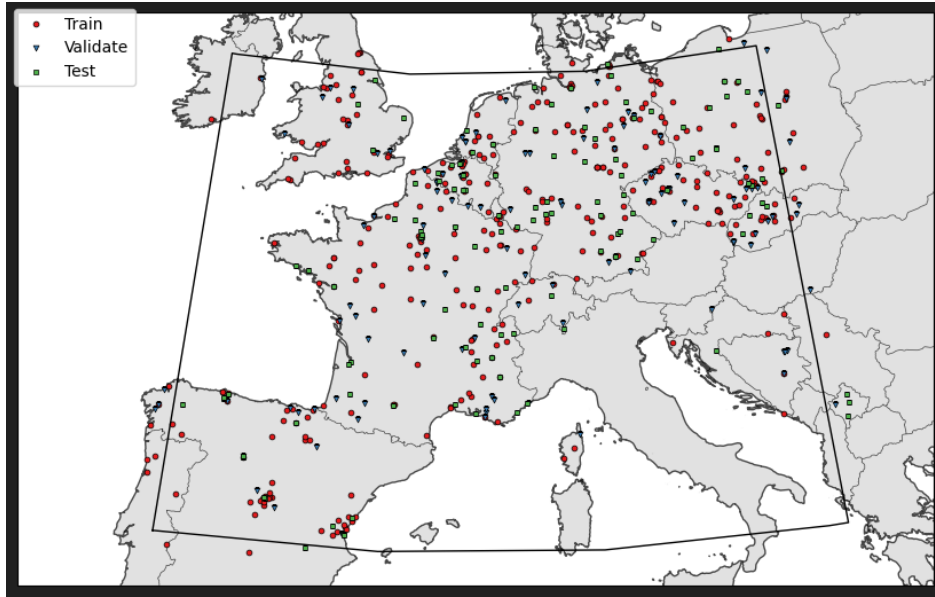


Figure 1. Map of stations in the region of interest.

3 Methods

165 3.1 AOD-to-PM_{2.5} conversion

Similarly as, for example, in van Donkelaar et al. (2021), we model the dependency between the PM_{2.5} at the surface level and AOD using the following model

$$\underline{PM}_{2.5} = \eta \cdot \underline{AOD}, \quad (5)$$

where $\eta = \eta(\mathbf{x}, t) = \eta(\mathbf{r}, t)$ is the AOD-to-PM_{2.5} conversion coefficient that is function of both time **and space** and space r.

170 3.2 Post-process correction approach

Let $y \in \mathbb{R}^m$ denote an accurate satellite retrieval

$$y = f(x), \quad (6)$$

where vector y contains the output of the satellite retrieval algorithm, $f : \mathbb{R}^n \mapsto \mathbb{R}^m$ is an accurate retrieval algorithm and $x \in \mathbb{R}^n$ contains all the algorithm inputs including the observation geometry and level 1 satellite observation data such as the top-of-atmosphere reflectances. The retrieval y can consist, for example, of surface PM_{2.5} at a given point in space and time.

In practice, due to uncertainties in the auxiliary parameters of the underlying forward model, extensive computational dimension of the problems and processing time limitations, it is not possible to construct an accurate retrieval algorithm f but an

approximate retrieval algorithm

$$\tilde{y} \approx \tilde{f}(x) \quad (7)$$

180 has to be employed instead. The approximate retrieval \tilde{f} is typically based on physically simplified and computationally reduced approximate forward models that are used due to [the](#) huge dimensionality of the retrieval problems and the need for computational efficiency. The utilization of the approximate retrieval algorithm leads to an *approximation error*

$$e(x) = f(x) - \tilde{f}(x) \quad (8)$$

in the retrieval parameters.

185 The core idea of the *model enforced* post-process correction model is to improve the accuracy of the approximate retrieval (7) by machine learning techniques. By Equations (6)-(8), the accurate retrieval can be written as

$$\begin{aligned} y &= f(x) \\ &= \tilde{f}(x) + [f(x) - \tilde{f}(x)] \\ &= \tilde{f}(x) + e(x). \end{aligned} \quad (9)$$

190 To obtain the corrected retrieval, Equation (9) is used to combine the conventional (physics-based) retrieval algorithm $\tilde{f}(x)$ and a machine learning based model $\hat{e}(x)$ to predict the realization of the approximation error $e(x)$ to obtain an corrected retrieval

$$y \approx \tilde{f}(x) + \hat{e}(x). \quad (10)$$

Note that this approach is different from a conventional *fully learned* machine learning model in which the aim is to emulate the accurate retrieval algorithm $f(x)$ with a machine learning model

$$195 \quad y \approx \hat{f}(x) \quad (11)$$

that is trained to predict the retrieval y directly from the satellite observation and geometry data x .

3.3 Correction of AOD-to-PM_{2.5} conversion factor η

In our work, we use the post-process correction approach (10) to correct for the MERRA-2-based AOD-to-PM_{2.5} conversion factor η . We utilize an ensemble of neural networks to learn the correction to the conversion factor η and producing simultaneously error envelopes related to the learning process. Our post process correction model ~~$\hat{e}(x)$~~ $\hat{e}(x) : \mathbb{R}^n \mapsto \mathbb{R}$ corrects the conversion factor pixel-by-pixel, meaning that

$$\hat{e}(x) : \mathbb{R}^n \mapsto \mathbb{R}.$$

$$\eta(x) \approx \hat{\eta} + \hat{e}(x) \quad (12)$$

$$205 \quad \text{PM}_{2.5} \approx \eta(x) \cdot \text{AOD}_{\text{POPCORN}} \quad (13)$$

where $\hat{\eta}$ represents the AOD-to-PM_{2.5} ratio to be corrected. The correction model is learned using collocated data from ground station PM_{2.5}-PM_{2.5} data, MERRA-2 data, satellite data and retrieval, meteorological data, and high-resolution geographical indicators. All the inputs used can be found in Table A1 and are described in Section 2. We used SHAP analysis (Lundberg and Lee, 2017) in order to estimate feature importance after the training of the model. In fig.A1 you can see a bar plot of the first 26 input features ordered by their importance (SHAP value) and in Table A1 the feature are ordered by their SHAP importance (from left to right and from top to bottom). Since no features showed non-negligible SHAP value, we decided to keep them all in the training of the model. We finally add the estimated correction term to the MERRA-2 η values and calculate the PM_{2.5} estimates corresponding to POPCORN AOD retrievals using Equation (5).

3.4 Selection of the network model

As the dimension n of the input data x to the correction model $\hat{e}(x)$ is relatively small ($n = 172$) and output is a scalar, we utilize a fully connected feedforward neural network for the regression task. The networks are implemented using the TensorFlow framework.

To optimize the neural network architecture, we employed KerasTuner, a hyperparameter optimization framework. The Adam optimizer and 10^{-3} learning rate were selected. We used the Mean Square Error (MSE) loss function in the training. Linear-A linear activation function was employed for the output layer as the correction $\hat{e}(x)$ is real valued. Other parameters, such as the activation functions and the number of nodes in hidden layers, were optimized using KerasTuner. We considered the number of hidden layers, experimenting with 2, 3, and 4-layer architectures. The model with two hidden layers led to slightly better accuracy compared to the deeper models with 3 or 4 hidden layers and thus we employed the architecture with two hidden layers as our final model. The final optimal neural network architecture comprises of 172 input features and two hidden layers with seLu activation functions. The first and second hidden layers consisted of 160 and 128 neurons, respectively. Figure 2 shows the neural network architecture obtained from the model optimization.

We divided the dataset into three subsets in training our neural network model. Specifically, 60% of the data was used for training, 20% for validation, and 20% for testing, see Figure 1 for the division of the AQ stations into the training, validation and test sites. The learning data was divided into training, validation and test data by stations instead of random division of data points in order to avoid model overfitting and having test data from locations within the region of interest that were not included in the model training. Figure 3 shows the proportions of different PM_{2.5} values in the train, validate and test data. We used the validation set and the early stopping technique with the patience of 30 to avoid overfitting of the neural network model.

In our tests, the model struggled to predict high PM_{2.5} values accurately. We partially attributed this limitation to the skewed distribution of our dataset, which was predominantly composed of low PM_{2.5} values, see Figure 3 for the histogram of the PM_{2.5} values of the AQ stations in the learning data. To address this, we introduced a cut-off value of $80 \mu\text{g m}^{-3}$ for PM_{2.5} and trained our model with samples corresponding to PM_{2.5} values only below this. Furthermore, we experimented with reweighting the loss function to emphasize higher PM_{2.5} values. Although this strategy slightly improved the model's performance on

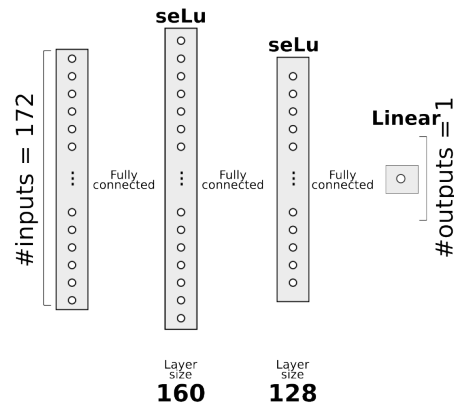


Figure 2. Feed-forward neural network architecture for post-process correction of η ratio, optimized with KerasTuner. The model contains two hidden layers with seLu activation functions (160 and 128 nodes respectively) and a single node output layer with linear activation function.

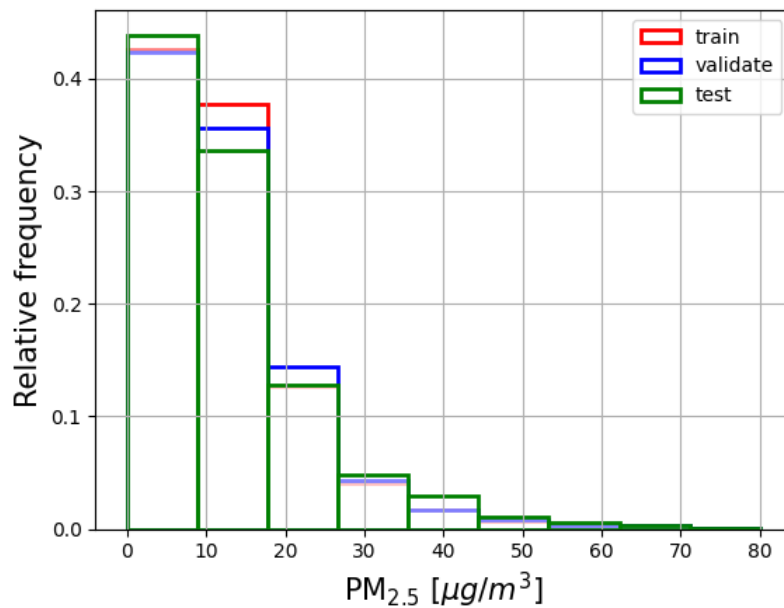


Figure 3. Distribution of AQ station $PM_{2.5}$ values in training, validation, and test sets. The training data is used to train the machine learning algorithm, while the validation data is used to prevent overfitting. The test data is used to test the results after training. The division of the data was obtained by dividing the AQ stations in the region of interest to three separate sets with 60%, 20% and 20% shares of training, validation and test stations.

the high-end tail, it compromised the accuracy on the low-end tail. Consequently, we decided not to use the reweighted loss
240 function.

3.5 Ensemble of networks

To address the problem of local minima and dependency on the initialization in neural network training we used an ensemble
based technique where we trained an ensemble of 80 networks each initialized with different random weights. We considered
the predictions of the networks as samples from a distribution and used the median of the predictions as a point estimate for
245 the correction term of η . We use the spread minimum to maximum interval of the 80 outputs of the networks as an learning
related uncertainty for η which was propagated onward to uncertainty of the $PM_{2.5}$ estimates through the conversion (5).

4 Results

Figure 4 shows scatter plots of the satellite and model-based predictions of $PM_{2.5}$ with respect to the values of the ground stations
for the test data AQ stations per single-overpass and as monthly averages. We calculated the monthly averages considering a
250 threshold: monthly averages were accepted only when we had more than 5 daily measurements per month (and station). The
figures on the top row show results for single-overpasses and the figures on the bottom row show monthly averages. The figures
on the left show the ground data ~~comparison-comparison~~ for the MERRA-2 $PM_{2.5}$ estimates, the figures on the middle show the
ground data ~~comparison-comparison~~ for the $PM_{2.5}$ values estimated using Equation (5) with POPCORN AOD and MERRA-
2 conversion factor η , and the figures on the right show the ~~comparison-comparison~~ for the $PM_{2.5}$ values estimated using
255 Equation (5) with POPCORN AOD and post-process corrected η . As can be seen, the use of post-process corrected conversion
factor leads to a clear improvement on the accuracy of the predictions of $PM_{2.5}$ at the independent test data locations. The R^2
coefficient ~~per single-overpass for instantaneous values~~ is improved by about ~~270%-290%~~ compared to both the MERRA-2
prediction and the estimate (5) with POPCORN AOD and MERRA-2 conversion factor; ~~the RMSE of~~. The RMSE is improved
by a factor 32% compared to MERRA-2 prediction and of by a factor 41% compared to the product of POPCORN AOD with
260 MERRA-2 η ; and the. The absolute value of the bias is reduced by a factor over 99%-95% respect to both of the uncorrected
estimates, and the MAE decreased by a factor 26% compared to MERRA-2 prediction and by a factor 41% compared to the
product of POPCORN AOD with MERRA-2 η . In the monthly averages the R^2 coefficient is improved by a factor ~~600%~~
~~350%~~ respect to MERRA-2 prediction and by a factor ~~250%-279%~~ compared to the estimate (5) with POPCORN AOD and
MERRA-2 η . The RMSE in the monthly averages is reduced by a factor ~~43%-over 47%~~ with respect to both uncorrected
265 methods. The bias in the monthly averages is reduced by a factor ~~83% and 76%, respectively~~ ~~92% and 89%, respectively, and~~
the MAE decreased by a factor 44% and 49%.

We remark that we tested also the fully-learned approach (11) for learning directly the AOD-to- $PM_{2.5}$ conversion factor η
values instead of the correction of the MERRA-2 based conversion, but the results with the fully learned approach were less
accurate than with the post-correction approach (10).

270 Figures 5 and 6 show $PM_{2.5}$ maps over Paris (23 February 2019) and Madrid (29 March 2019) for a single satellite overpass, respectively. On the top-left the uncorrected map is obtained based on POPCORN AOD ~~550nm~~-500nm and MERRA-2 η , while on the top-right the corrected map uses the post-process corrected MERRA-2 η . On the bottom left we compare the satellite based $PM_{2.5}$ values to the measured $PM_{2.5}$ values at the AQ stations which are represented by the circles in the maps. The red circles represent the post-corrected estimates (medians calculated from the ensemble predictions), the black dots the uncorrected estimates while the blue dots the ground based measurement values at the stations. The red error bars represent the spread of $PM_{2.5}$ values coming from the ensemble of networks and they are to be considered as uncertainty estimates related to the machine learning process. The joint RMSE of the uncorrected estimates with respect to the ground stations are ~~8.26~~ 7.82 $\mu g/m^3$ and ~~5.17~~ 4.59 $\mu g/m^3$ respectively for Paris and Madrid, and the joint RMSE for the post-corrected estimates with respect the ground stations are ~~7.86~~ 6.36 $\mu g/m^3$ and ~~4.93~~ 2.27 $\mu g/m^3$, indicating improved accuracy of the per overpass $PM_{2.5}$ estimates in the post process correction approach. The figure reveals that, for all the stations, the different initialization points for the trainings improve over the uncorrected prediction. The median of the ensemble predictions is not always better than the uncorrected prediction, but the uncertainty interval is either enclosing the measured value or is closer to the measured value than the uncorrected estimate. The bottom right images show a time series of $PM_{2.5}$ monthly averages predictions against the time series coming from a ground station monthly averages (the stations are pointed on the corrected maps by a white arrow). The red envelopes show the uncertainty envelope of the post-process corrected estimate. Here the ground station monthly averages are contained in the uncertainty envelope. Figure 7 shows time series of $PM_{2.5}$ monthly averages of the post-process corrected estimates for different stations in the region of interest, showing good alignment with the accurate ground based AQ measurements. Similar performance was found out for the monthly averages in most of the test stations in the region of interest, indicating that the post process corrected estimates of monthly averages of $PM_{2.5}$ are generally well aligned with the accurate ground based observations.

290 The post process correction method we have proposed here is flexible with respect data to be utilized in the training, as it allows straightforward addition of more training data (by re-optimization of the neural network architecture) coming from different data sources in order to improve the $PM_{2.5}$ predictions. In this study, we demonstrated the approach using POPCORN AOD data, which is obtained post-correcting Sentinel-3 AOD. The approach can also be extended and trained to other satellite instruments and their AOD products to obtain similarly post-process corrected high-resolution satellite estimates of $PM_{2.5}$, leading to more frequent temporal sampling of a particular location. In this study, we demonstrated the approach using a relatively large region-of-interest covering central Europe year 2019. The approach can also be scaled in a straightforward manner to smaller or larger regions of interest by changing the training data.

5 Conclusions

300 We developed an innovative machine learning technique aimed at correcting the AOD-to- $PM_{2.5}$ ratio derived from MERRA-2 data. This correction method integrates data from various sources, including ground station $PM_{2.5}$ data, MERRA-2 data, satellite data, meteorological data, and high-resolution geographical indicators. The post process corrected AOD-to- PM ratio

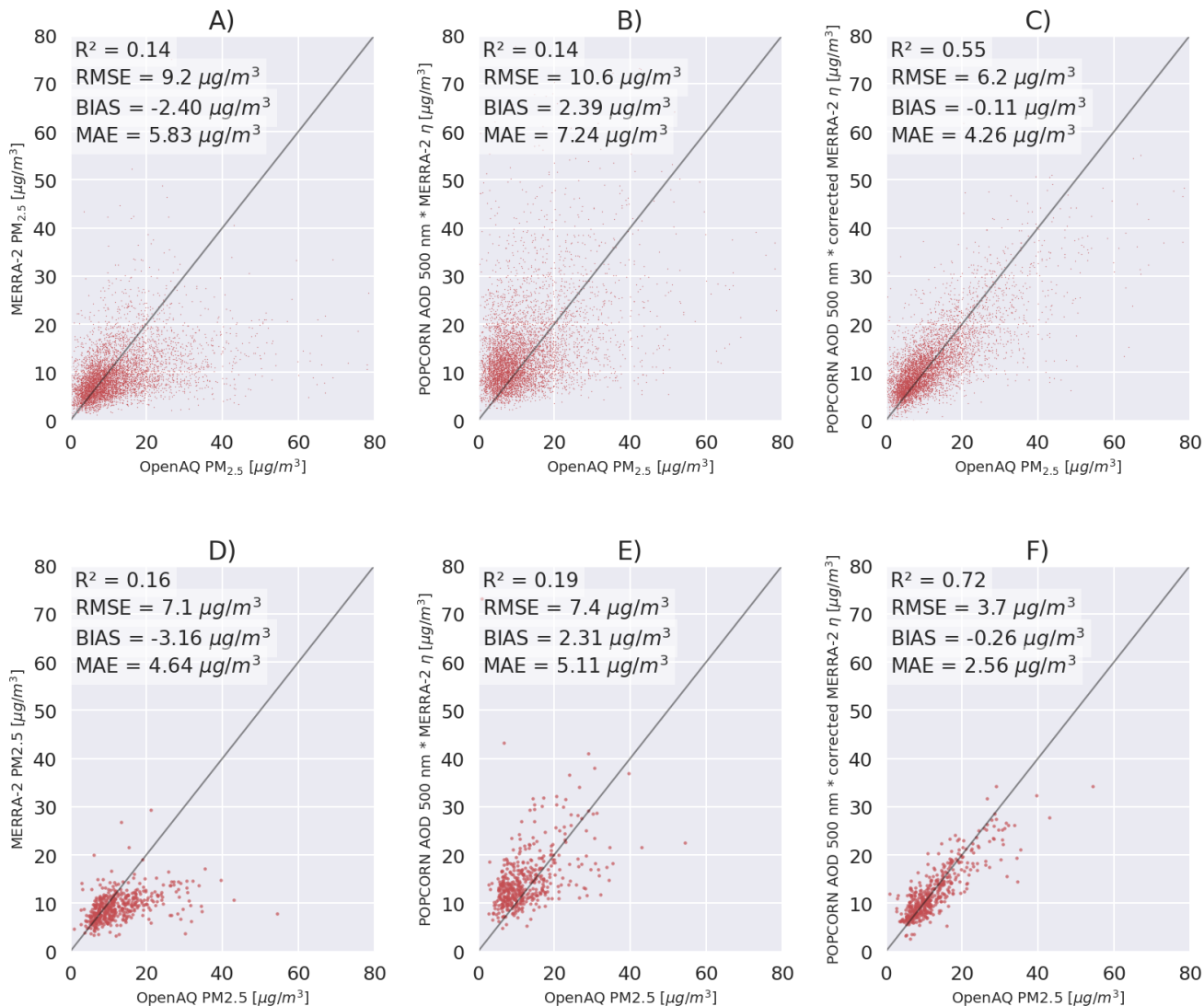


Figure 4. A) MERRA-2 PM_{2.5} predictions against OpenAQ PM_{2.5} measurements per single-overpass. B) Uncorrected NOODLESALAD PM_{2.5} predictions against OpenAQ PM_{2.5} measurements per single-overpass. C) Corrected NOODLESALAD PM_{2.5} predictions against OpenAQ PM_{2.5} measurements per single-overpass. D) MERRA-2 monthly averages PM_{2.5} predictions against OpenAQ monthly averages PM_{2.5} measurements. E) Uncorrected NOODLESALAD monthly averages PM_{2.5} predictions against OpenAQ monthly averages PM_{2.5} measurements. F) Corrected NOODLESALAD monthly averages PM_{2.5} predictions against OpenAQ monthly averages PM_{2.5} measurements.

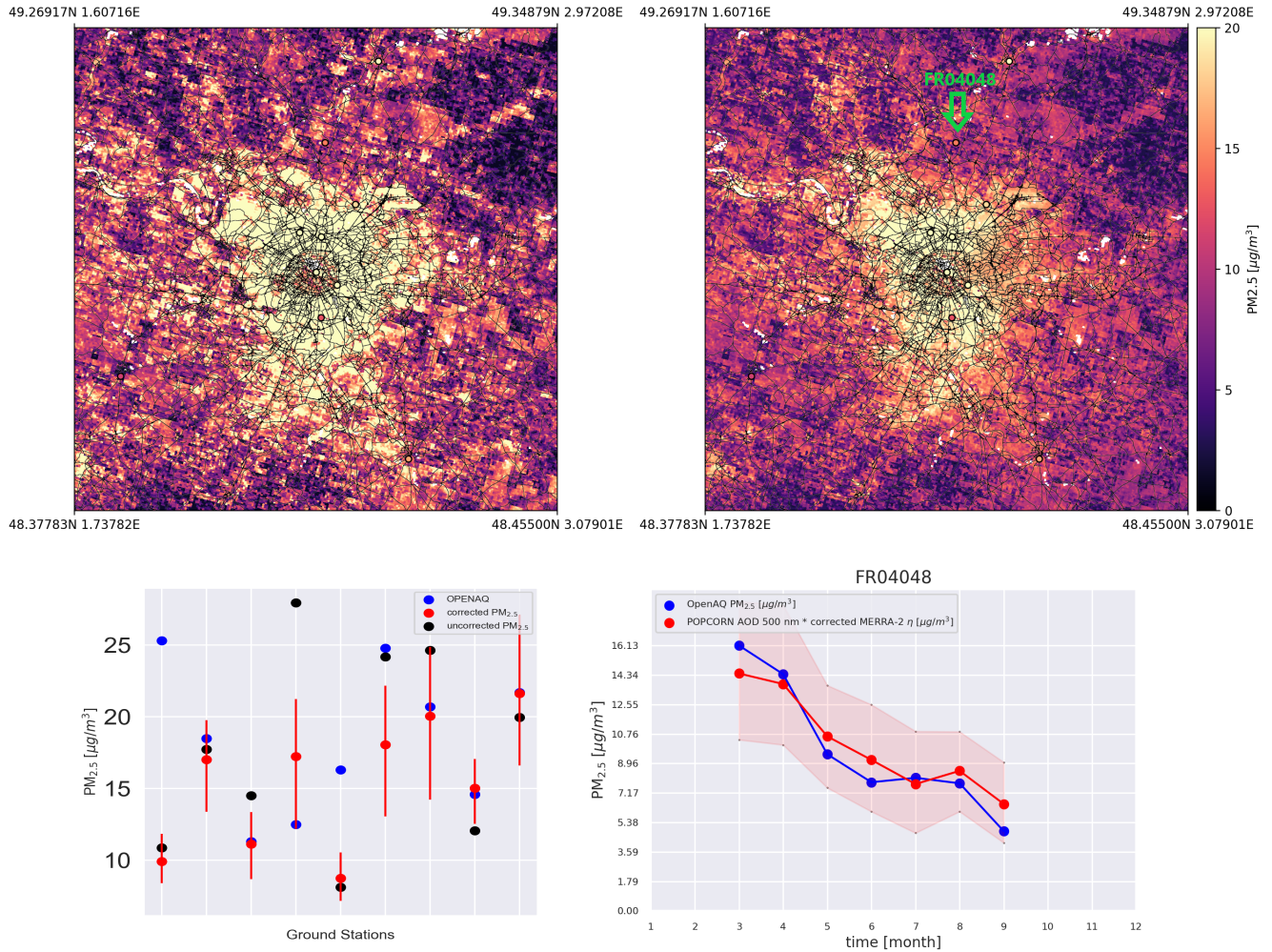


Figure 5. On the top-left: single overpass not-corrected PM_{2.5} map over Paris (RMSE against ground stations = ~~8.26~~7.82 $\mu\text{g}/\text{m}^3$). On the top-right: single overpass corrected PM_{2.5} map over Paris (RMSE against ground stations = ~~7.86~~6.36 $\mu\text{g}/\text{m}^3$). Notice that the white regions for the figures on top are regions where the AOD (so the PM_{2.5}) values are missing because of cloud contamination. On the bottom-left: comparison of the uncorrected and corrected method at the ground stations, The red error bars represent the spread of values obtained through the ensemble method, while the red dots represent the medians of those values. On the bottom-right: comparison between OpenAQ and corrected method predicted time series of PM_{2.5} monthly averages at a single station (indicated on the corrected map by a ~~white~~green arrow). The red envelope represents the uncertainty coming from the ensemble method.

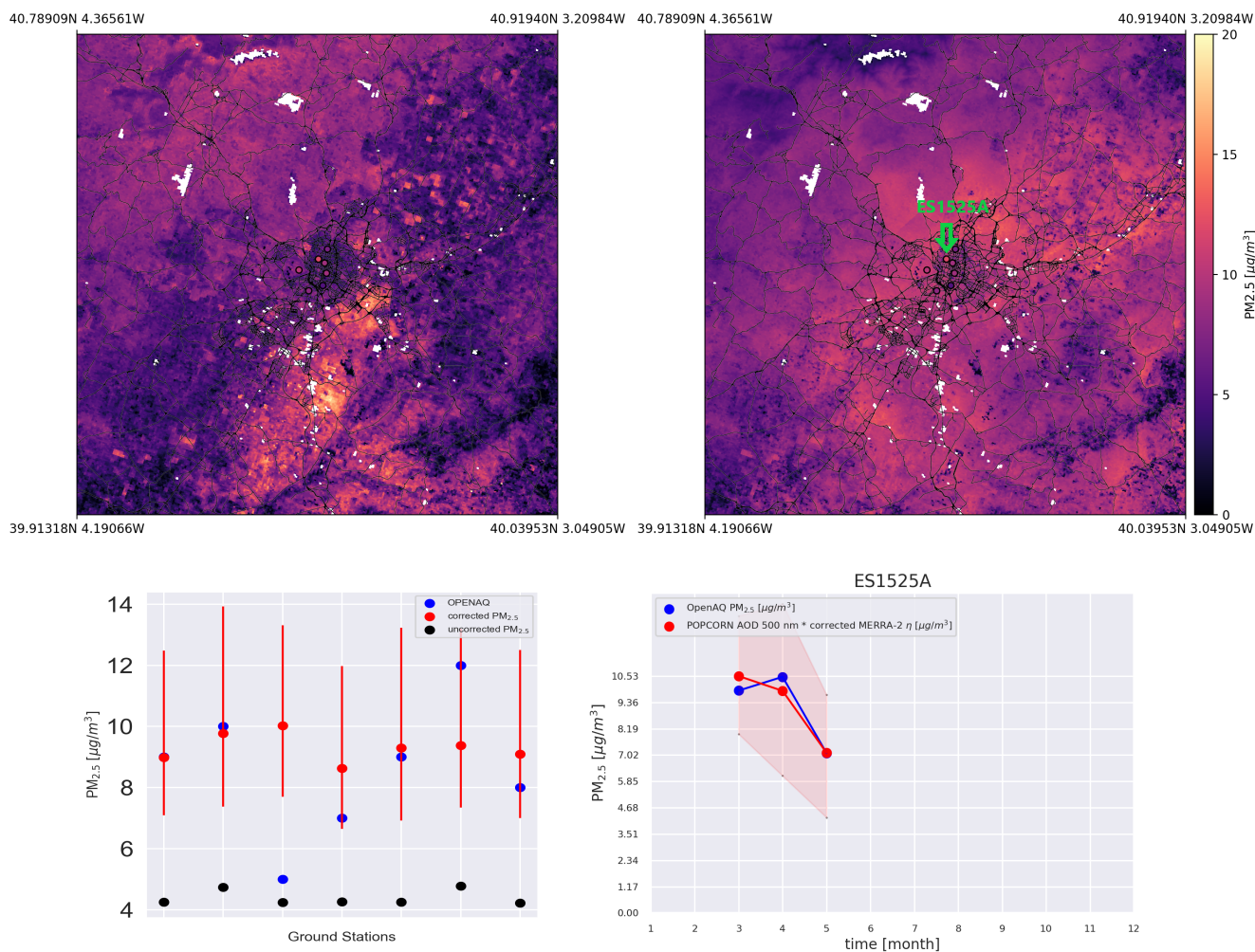


Figure 6. On the top-left: single overpass not-corrected PM_{2.5} map over Madrid (RMSE against ground stations = ~~5.17~~ 4.59 $\mu\text{g}/\text{m}^3$). On the top-right: single overpass corrected PM_{2.5} map over Madrid (RMSE against ground stations = ~~1.93~~ 2.27 $\mu\text{g}/\text{m}^3$). Notice that the white regions for the figures on top are regions where the AOD (so the PM_{2.5}) values are missing because of cloud contamination. On the bottom-left: comparison of the uncorrected and corrected method at the ground stations. The red error bars represent the spread of values obtained through the ensemble method, while the red dots represent the medians of those values. On the bottom-right: comparison between OpenAQ and corrected method predicted time series of PM_{2.5} monthly averages at a single station (indicated on the corrected map by a ~~white~~ green arrow). The red envelope represents the uncertainty coming from the ensemble method.

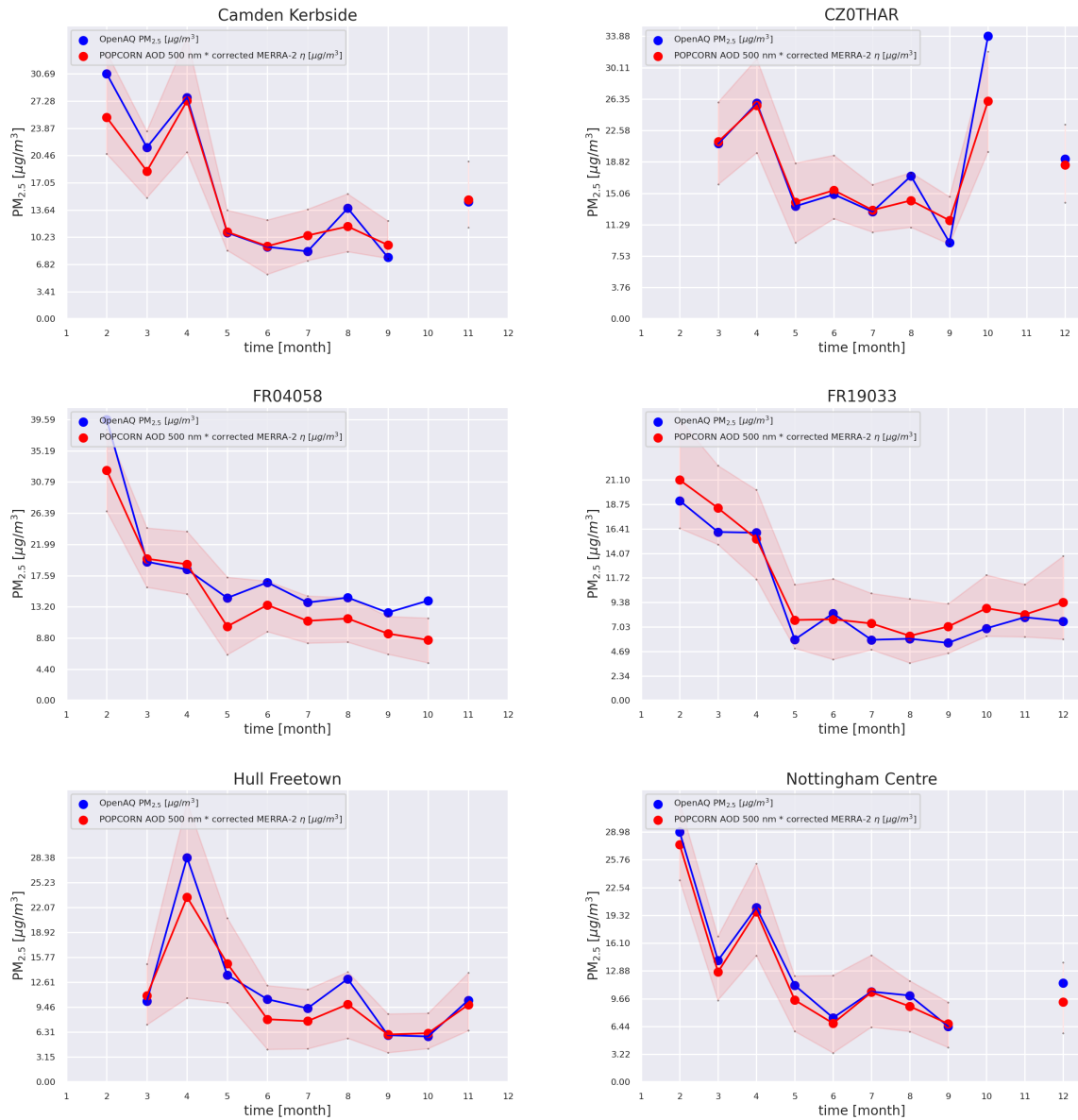


Figure 7. Monthly averages time series for six stations from the independent test set within the region of interest. The red envelopes represent the uncertainty coming from the ensemble method.

was then employed to estimate $PM_{2.5}$ levels within the Central Europe region for the year 2019. Our approach outperforms MERRA-2 predictions and predictions made using MERRA-2 AOD-to-PM ratio and POPCORN AOD, resulting in improvement in all evaluated metrics, whether considering individual overpasses or monthly averages. The $PM_{2.5}$ estimates were derived by aggregating the median values from an ensemble of neural networks. We incorporated the ensemble's value spread as a measure of machine learning related uncertainty in the post-process corrected $PM_{2.5}$ estimates, and our estimates with their uncertainty envelopes were found to be generally highly feasible with respect the accurate ground based observations at the independent test station locations. We remark that while our approach produced generally good accuracy in estimation of $PM_{2.5}$, it exhibited poorer performance for the high end values of $PM_{2.5}$. This finding can be attributed to small number of learning data for the high end tail of $PM_{2.5}$ values in our region of interest, highlighting the obvious fact that the learning data for machine learning needs to be representative for the operational environment and conditions.

In this study, our goal was to utilize a simple neural network model to estimate the $PM_{2.5}$ values from satellite data. Therefore, the adoption of a fully connected neural network architecture was considered a reasonable choice. The architecture of the network was determined through a combination of manual selection and the use of KerasTuner to optimize the number of neurons per layer and the activation function. This ensured the development of an effective network for the specific problem under study. The robust performance of the resulting model highlights the efficacy of employing a simple neural network model to address $PM_{2.5}$ estimation with notable success.

Code and data availability. Sentinel-3 Synergy Land POPCORN dataset is openly available for download at https://a3s.fi/swift/v1/AUTH_ca5072b7b22e463b85a2739fd6cd5732/POPCORNdata/readme.html. The OpenAQ data is open data and available for download at <https://openaq.org/>. The OpenStreetMap data is open data and available for download at <https://www.openstreetmap.org/>. All the NASA data (MERRA-2, CALIOP, MODIS, ASTER DEM) used in this work is open data and can be found and downloaded using the NASA Earthdata Search website at <https://www.earthdata.nasa.gov/>. The NASA Black Marble Night Lights data is available at <https://blackmarble.gsfc.nasa.gov/>. Code will be available from the authors on a reasonable request.

Author contributions. **Andrea Porcheddu:** Conceptualization, Methodology, Software, Formal analysis, Writing — Original draft, Visualization **Ville Kolehmainen:** Conceptualization, Methodology, Formal analysis, Writing — Original draft, Supervision **Timo Lähivaara:** Conceptualization, Methodology, Formal analysis, Writing - Original Draft, Supervision **Antti Lipponen:** Conceptualization, Methodology, Software, Formal analysis, Writing — Original draft, Visualization, Supervision

Competing interests. The authors declare no competing interests.

330 *Acknowledgements.* This study was funded by the European Space Agency EO Science for Society programme via the NOODLESALAD project (contract number 4000137651/22/I-DT-Ir). The research was also supported by the ~~Academy of Finland, the~~ Finnish Centre of Excellence of Inverse Modelling and Imaging (project no. ~~336791~~)~~and the Academy-353084~~, [Flagship of Advanced Mathematics for Sensing Imaging and Modelling \(grant no. 358944\)](#), and the [Research Council](#) of Finland (project no. 321761). The authors wish to acknowledge CSC – IT Center for Science, Finland, for computational resources.

335 Appendix A: Lists of variables used from datasets

A1 MERRA-2 variables

We use the following meteorology-related variables from the MERRA-2 M2T1NXSLV dataset:

- **PS**: surface pressure (Pa)
- **QV10M**: 10-meter specific humidity (kg kg^{-1})
- 340 – **QV2M**: 2-meter specific humidity (kg kg^{-1})
- **SLP**: sea level pressure (Pa)
- **T10M**: 10-meter air temperature (K)
- **T2M**: 2-meter air temperature (K)
- **TO3**: total column ozone (Dobsons)
- 345 – **TOX**: total column odd oxygen (kg m^{-2})
- **TQI**: total precipitable ice water (kg m^{-2})
- **TQL**: total precipitable liquid water (kg m^{-2})
- **TQV**: total precipitable water vapor (kg m^{-2})
- **TROPPB**: tropopause pressure based on blended estimate (Pa)
- 350 – **TROPPT**: tropopause pressure based on thermal estimate (Pa)
- **TROPPV**: tropopause pressure based on EPV estimate (Pa)
- **TROPQ**: tropopause specific humidity using blended TROPP estimate (kg kg^{-1})
- **TROPT**: tropopause temperature using blended TROPP estimate (K)
- **TS**: surface skin temperature (K)
- 355 – **U10M**: 10-meter eastward wind (m / s)
- **U2M**: 2-meter eastward wind (m / s)
- **U50M**: eastward wind at 50 meters (m / s)
- **V10M**: 10-meter northward wind (m / s)

– **V2M**: 2-meter northward wind (m / s)

360 – **V50M**: northward wind at 50 meters (m / s)

We use the following meteorology-related variables from the MERRA-2 M2T1NXFLX dataset:

– **BSTAR**: surface bouyancy scale (m s^{-2})

– **CDH**: surface exchange coefficient for heat ($\text{kg m}^{-2} \text{s}^{-1}$)

– **CDM**: surface exchange coefficient for momentum ($\text{kg m}^{-2} \text{s}^{-1}$)

365 – **CDQ**: surface exchange coefficient for moisture ($\text{kg m}^{-2} \text{s}^{-1}$)

– **CN**: surface neutral drag coefficient (1)

– **DISPH**: zero plane displacement height (m)

– **EFLUX**: total latent energy flux (W m^{-2})

– **EVAP**: evaporation from turbulence ($\text{kg m}^{-2} \text{s}^{-1}$)

370 – **FRCAN**: areal fraction of anvil showers (1)

– **FRCCN**: areal fraction of convective showers (1)

– **FRCLS**: areal fraction of nonanvil large scale showers (1)

– **FRSEAIICE**: ice covered fraction of tile (1)

– **GHTSKIN**: ground heating for skin temp (W m^{-2})

375 – **HFLUX**: sensible heat flux from turbulence (W m^{-2})

– **HLML**: surface layer height (m)

– **NIRDF**: surface downwelling nearinfrared diffuse flux (W m^{-2})

– **NIRDR**: surface downwelling nearinfrared beam flux (W m^{-2})

– **PBLH**: planetary boundary layer height (m)

380 – **PGENTOT**: total column production of precipitation ($\text{kg m}^{-2} \text{s}^{-1}$)

– **PRECANV**: anvil precipitation ($\text{kg m}^{-2} \text{s}^{-1}$)

– **PRECCON**: convective precipitation ($\text{kg m}^{-2} \text{s}^{-1}$)

- **PRECLSC**: nonanvil large scale precipitation ($\text{kg m}^{-2} \text{s}^{-1}$)
- **PRECSNO**: snowfall ($\text{kg m}^{-2} \text{s}^{-1}$)
- 385 – **PRECTOT**: total precipitation from atm model physics ($\text{kg m}^{-2} \text{s}^{-1}$)
- **PRECTOTCORR**: Bias corrected total precipitation ($\text{kg m}^{-2} \text{s}^{-1}$)
- **PREVTOT**: total column re-evap/subl of precipitation ($\text{kg m}^{-2} \text{s}^{-1}$)
- **QLML**: surface specific humidity (1)
- **QSH**: effective surface specific humidity (kg kg^{-1})
- 390 – **QSTAR**: surface moisture scale (kg kg^{-1})
- **RHOA**: air density at surface (kg m^{-3})
- **RISFC**: surface bulk Richardson number (1)
- **SPEED**: surface wind speed (m s^{-1})
- **SPEEDMAX**: surface wind speed (m s^{-1})
- 395 – **TAUGWX**: surface eastward gravity wave stress (N m^{-2})
- **TAUGWY**: surface northward gravity wave stress (N m^{-2})
- **TAUX**: eastward surface stress (N m^{-2})
- **TAUY**: northward surface stress (N m^{-2})
- **TCZPBL**: transcom planetary boundary layer height (m)
- 400 – **TLML**: surface air temperature (K)
- **TSH**: effective surface skin temperature (K)
- **TSTAR**: surface temperature scale (K)
- **ULML**: surface eastward wind (m s^{-1})
- **USTAR**: surface velocity scale (m s^{-1})
- 405 – **VLML**: surface northward wind (m s^{-1})
- **Z0H**: surface roughness for heat (m)

- **Z0M**: surface roughness (m)

We use the following aerosol and air quality related variables from the MERRA-2 M2T1NXAER dataset:

- **BCANGSTR**: Black Carbon Angstrom parameter [470-870 nm] (1)
- 410 – **BCCMASS**: Black Carbon Column Mass Density (kg m^{-2})
- **BCEXTTAU**: Black Carbon Extinction AOT [550 nm] (1)
- **BCFLUXU**: Black Carbon column u-wind mass flux ($\text{kg m}^{-1} \text{s}^{-1}$)
- **BCFLUXV**: Black Carbon column v-wind mass flux ($\text{kg m}^{-1} \text{s}^{-1}$)
- **BCSCATAU**: Black Carbon Scattering AOT [550 nm] (1)
- 415 – **BCSMASS**: Black Carbon Surface Mass Concentration (kg m^{-3})
- **DMSCMASS**: DMS Column Mass Density (kg m^{-2})
- **DMSSMASS**: DMS Surface Mass Concentration (kg m^{-3})
- **DUANGSTR**: Dust Angstrom parameter [470-870 nm] (1)
- **DUCMASS**: Dust Column Mass Density (kg m^{-2})
- 420 – **DUCMASS25**: Dust Column Mass Density - PM 2.5 (kg m^{-2})
- **DUEXTT25**: Dust Extinction AOT [550 nm] - PM 2.5 (1)
- **DUEXTTAU**: Dust Extinction AOT [550 nm] (1)
- **DUFLUXU**: Dust column u-wind mass flux ($\text{kg m}^{-1} \text{s}^{-1}$)
- **DUFLUXV**: Dust column v-wind mass flux ($\text{kg m}^{-1} \text{s}^{-1}$)
- 425 – **DUSCAT25**: Dust Scattering AOT [550 nm] - PM 2.5 (1)
- **DUSCATAU**: Dust Scattering AOT [550 nm] (1)
- **DUSMASS**: Dust Surface Mass Concentration (kg m^{-3})
- **DUSMASS25**: Dust Surface Mass Concentration - PM 2.5 (kg m^{-3})
- **OCANGSTR**: Organic Carbon Angstrom parameter [470-870 nm] (1)
- 430 – **OCCMASS**: Organic Carbon Column Mass Density (kg m^{-2})

- **OCEXTTAU**: Organic Carbon Extinction AOT [550 nm] (1)
- **OCFLUXU**: Organic Carbon column u-wind mass flux ($\text{kg m}^{-1} \text{s}^{-1}$)
- **OCFLUXV**: Organic Carbon column v-wind mass flux ($\text{kg m}^{-1} \text{s}^{-1}$)
- **OCSCATAU**: Organic Carbon Scattering AOT [550 nm] (1)
- 435 – **OCSMASS**: Organic Carbon Surface Mass Concentration (kg m^{-3})
- **SO2CMASS**: SO2 Column Mass Density (kg m^{-2})
- **SO2SMASS**: SO2 Surface Mass Concentration (kg m^{-3})
- **SO4CMASS**: SO4 Column Mass Density (kg m^{-2})
- **SO4SMASS**: SO4 Surface Mass Concentration (kg m^{-3})
- 440 – **SSANGSTR**: Sea Salt Angstrom parameter [470-870 nm] (1)
- **SSCMASS**: Sea Salt Column Mass Density (kg m^{-2})
- **SSCMASS25**: Sea Salt Column Mass Density - PM 2.5 (kg m^{-2})
- **SSEXTT25**: Sea Salt Extinction AOT [550 nm] - PM 2.5 (1)
- **SSEXTTAU**: Sea Salt Extinction AOT [550 nm] (1)
- 445 – **SSFLUXU**: Sea Salt column u-wind mass flux ($\text{kg m}^{-1} \text{s}^{-1}$)
- **SSFLUXV**: Sea Salt column v-wind mass flux ($\text{kg m}^{-1} \text{s}^{-1}$)
- **SSSCAT25**: Sea Salt Scattering AOT [550 nm] - PM 2.5 (1)
- **SSSCATAU**: Sea Salt Scattering AOT [550 nm] (1)
- **SSSMASS**: Sea Salt Surface Mass Concentration (kg m^{-3})
- 450 – **SSSMASS25**: Sea Salt Surface Mass Concentration - PM 2.5 (kg m^{-3})
- **SUANGSTR**: SO4 Angstrom parameter [470-870 nm] (1)
- **SUEXTTAU**: SO4 Extinction AOT [550 nm] (1)
- **SUFLUXU**: SO4 column u-wind mass flux ($\text{kg m}^{-1} \text{s}^{-1}$)
- **SUFLUXV**: SO4 column v-wind mass flux ($\text{kg m}^{-1} \text{s}^{-1}$)

- 455 – **SUSCATAU**: SO4 Scattering AOT [550 nm] (1)
- **TOTANGSTR**: Total Aerosol Angstrom parameter [470-870 nm] (1)
- **TOTEXTTAU**: Total Aerosol Extinction AOT [550 nm] (1)
- **TOTSCATAU**: Total Aerosol Scattering AOT [550 nm] (1)

A2 OpenStreetMap road types used to compute the distance to the closest road

460 We use the following road types to compute the distance to the closest road. The descriptions of the road types are obtained from OpenStreetMap (2023).

- **motorway**: A restricted access major divided highway, normally with 2 or more running lanes plus emergency hard shoulder. Equivalent to the Freeway, Autobahn, etc.
- **trunk**: The most important roads in a country's system that aren't motorways.
- 465 – **primary**: The next most important roads in a country's system.
- **secondary**: The next most important roads in a country's system.
- **tertiary**: The next most important roads in a country's system.
- **motorway_link**: The link roads (sliproads/ramps) leading to/from a motorway from/to a motorway or lower class highway. Normally with the same motorway restrictions.
- 470 – **trunk_link**: The link roads (sliproads/ramps) leading to/from a trunk road from/to a trunk road or lower class highway.
- **primary_link**: The link roads (sliproads/ramps) leading to/from a primary road from/to a primary road or lower class highway.
- **secondary_link**: The link roads (sliproads/ramps) leading to/from a secondary road from/to a secondary road or lower class highway.
- 475 – **tertiary_link**: The link roads (sliproads/ramps) leading to/from a tertiary road from/to a tertiary road or lower class highway.

A3 IGBP land cover types

IGBP classification contains the following land cover types:

- **1**: Evergreen needleleaf forests
- 480 – **2**: Evergreen broadleaf forests

- 3: Deciduous needleleaf forests
- 4: Deciduous broadleaf forests
- 5: Mixed forests
- 6: Closed shrublands
- 485 – 7: Open shrublands
- 8: Woody savannas
- 9: Savannas
- 10: Grasslands
- 11: Permanent wetlands
- 490 – 12: Croplands
- 13: Urban and built-up
- 14: Cropland/natural
- 15: Snow and ice
- 16: Barren
- 495 – 17: Water bodies

A4 Table of all input variables

MERRA2_POPCORN_ELEVATIONDIFFERENCE	POPCORN_AOD500	POPCORN_AOD870
MERRA2_ETA	MERRA2_FLX_GHTSKIN	POPCORN_distancetolandclass2
POPCORN_time_cyclic_yearly_sin	POPCORN_time_cyclic_yearly_cos	POPCORN_AOD675
MERRA2_surface_to_column_ratio_PM25	POPCORN_AOD550	MERRA2_ASMCONST_SGH
POPCORN_distancetolandclass6	MERRA2_AER_BCFLUXU	MERRA2_AER_SO2CMASS
MERRA2_ASM_QV2M	POPCORN_ANGSTROM	MERRA2_AER_DUSMASS
MERRA2_AER_SSSMASS25	POPCORN_AOD440	MERRA2_ASM_TROPT
MERRA2_AER_TOTANGSTR	MERRA2_ASM_QV10M	MERRA2_ASM_T2M
MERRA2_AER_OCCMASS	MERRA2_ASM_TQV	MERRA2_FLX_QLML
MERRA2_AER_SUFLUXV	MERRA2_FLX_USTAR	MERRA2_AER_SO4CMASS
POPCORN_distancetolandclass17	MERRA2_AER_DUCMASS	MERRA2_AER_BCSMASS
MERRA2_AER_BCSCATAU	MERRA2_AER_DUEXTTAU	MERRA2_FLX_EFLUX
MERRA2_AER_SO4SMASS	MERRA2_FLX_EVAP	MERRA2_FLX_NIRDR
MERRA2_FLX_HFLUX	POPCORN_ASTERDEM	MERRA2_AER_SUANGSTR
MERRA2_ASM_TROPPB	MERRA2_AER_BCFLUXV	MERRA2_FLX_TLML
MERRA2_FLX_QSTAR	POPCORN_time_cyclic_daily_sin	MERRA2_AER_DUSCATAU
MERRA2_FLX_PBLH	POPCORN_distancetolandclass7	POPCORN_distancetolandclass12
MERRA2_AER_OCSCATAU	MERRA2_AER_TOTEXTTAU	POPCORN_distancetolandclass15
MERRA2_ASM_TROPPV	MERRA2_SURFACERH	MERRA2_FLX_RHOA
MERRA2_AER_BCEXTTAU	MERRA2_FLX_FRCLS	MERRA2_AER_DUEXTT25
MERRA2_ASM_T10M	MERRA2_ASM_TS	MERRA2_FLX_SPEED
MERRA2_AER_BCANGSTR	MERRA2_AER_DUSCAT25	MERRA2_AER_OCFLUXU
MERRA2_CTMCONST_FRLANDICE	MERRA2_AER_DUCMASS25	MERRA2_AER_OCEXTTAU
MERRA2_FLX_FRCAN	MERRA2_ASMCONST_FRLAND	MERRA2_AER_SSCMASS
MERRA2_AER_TOTSCATAU	MERRA2_AER_BCCMASS	MERRA2_CTMCONST_FRACI
MERRA2_AER_DUSMASS25	POPCORN_distancetolandclass16	POPCORN_CALIOP_MASK_AOD_90_Percent_Below
POPCORN_time_cyclic_daily_cos	POPCORN_distancetolandclass4	MERRA2_AER_DUANGSTR
MERRA2_FLX_SPEEDMAX	MERRA2_CTMCONST_FRLAND	MERRA2_FLX_HLML
MERRA2_AER_DUFLUXV	MERRA2_AER_OCANGSTR	MERRA2_FLX_TAU
MERRA2_FLX_FRCCN	MERRA2_PM25	MERRA2_ASMCONST_FRLAKE
POPCORN_distancetolandclass8	MERRA2_AER_SSFLUXV	MERRA2_AER_SUFLUXU
MERRA2_FLX_CDQ	POPCORN_distancetolandclass13	MERRA2_FLX_TSTAR
MERRA2_FLX_CN	MERRA2_ASM_V50M	MERRA2_AER_SSSCATAU
MERRA2_FLX_QSH	MERRA2_FLX_Z0H	MERRA2_ASM_PS
MERRA2_AER_SSEXTTAU	MERRA2_FLX_TCZPBL	MERRA2_AER_OCSMASS
MERRA2_FLX_TSH	POPCORN_distancetolandclass3	MERRA2_SURFACEELEVATION
MERRA2_ASM_TROPQ	MERRA2_FLX_CDH	MERRA2_FLX_PGENTOT
MERRA2_ASM_U10M	MERRA2_FLX_ULML	MERRA2_ASM_TOX
MERRA2_AER_DMSCMASS	POPCORN_distancetolandclass1	POPCORN_distancetolandclass14
MERRA2_FLX_TAU	MERRA2_ASMCONST_FRLANDICE	MERRA2_AER_SUSCATAU
MERRA2_AER_DUFLUXU	POPCORN_distancetolandclass10	MERRA2_FLX_PREVTOT
MERRA2_CTMCONST_FROCEAN	MERRA2_ASM_TQL	MERRA2_ASM_U2M
MERRA2_ASM_DISPH	MERRA2_FLX_PRECTOT	MERRA2_AER_SO2SMASS
MERRA2_FLX_CDM	MERRA2_FLX_Z0M	MERRA2_ASM_windspeed
POPCORN_distancetolandclass11	MERRA2_FLX_DISPH	MERRA2_AER_OCFLUXV
MERRA2_FLX_PRECTOTCORR	MERRA2_ASM_TROPPT	MERRA2_FLX_PRECLSC
MERRA2_FLX_BSTAR	MERRA2_ASM_TO3	POPCORN_CALIOP_MASK_AOD_63_Percent_Below
MERRA2_FLX_PRECCON	MERRA2_ASM_TQI	MERRA2_ASMCONST_FROCEAN
MERRA2_CTMCONST_PHIS	POPCORN_distancetolandclass5	MERRA2_CTMCONST_FRLAKE
MERRA2_FLX_TAUWX	MERRA2_FLX_PRECANV	MERRA2_ASM_V2M
MERRA2_ASMCONST_PHIS	MERRA2_FLX_NIRDF	POPCORN_distancetolandclass9
MERRA2_ASM_SLP	POPCORN_BlackMarble	POPCORN_distancetoroad_upwind
MERRA2_AER_SSANGSTR	MERRA2_FLX_VLML	MERRA2_AER_SSSCAT25
MERRA2_ASM_windirection	MERRA2_FLX_TAUWY	MERRA2_AER_SSFLUXU
MERRA2_AER_SUEXTTAU	MERRA2_ASM_V10M	MERRA2_AER_SSCMASS25
MERRA2_FLX_PRECSNO	MERRA2_AER_SSEXTT25	MERRA2_AER_DMSSMASS
MERRA2_FLX_RISFC	MERRA2_AER_SSSMASS	MERRA2_ASM_U50M
MERRA2_FLX_FRSEAICE		

Table A1. List of input variables used in our model ordered by SHAP value (from left to right and from top to bottom).

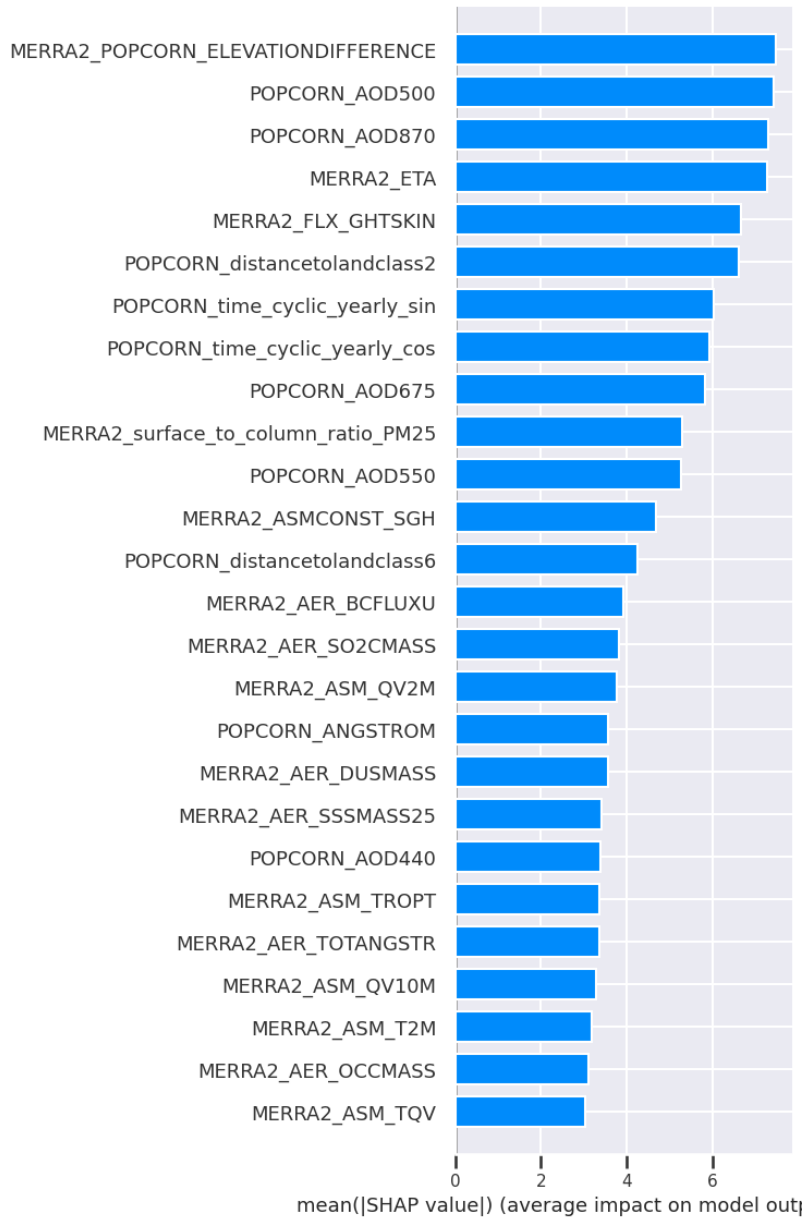


Figure A1. [Bar plot of the SHAP values for the first 26 input variables in order of importance.](#)

References

Belward, A. S., Estes, J. E., and Kline, K. D.: The IGBP-DIS global 1-km land-cover data set DISCover: A project overview, *Photogrammetric Engineering and Remote Sensing*, 65, 1013–1020, 1999.

- 500 Buchard, V., Da Silva, A., Randles, C., Colarco, P., Ferrare, R., Hair, J., Hostetler, C., Tackett, J., and Winker, D.: Evaluation of the surface PM_{2.5} in Version 1 of the NASA MERRA Aerosol Reanalysis over the United States, *Atmospheric Environment*, 125, 100–111, 2016.
- Cohen, A. J., Brauer, M., Burnett, R., Anderson, H. R., Frostad, J., Estep, K., et al.: Estimates and 25-year trends of the global burden of disease attributable to ambient air pollution: an analysis of data from the Global Burden of Diseases Study 2015, *The Lancet*, 389, 1907–1918, 2017.
- 505 Fujisada, H., Urai, M., and Iwasaki, A.: Advanced methodology for ASTER DEM generation, *IEEE transactions on geoscience and remote sensing*, 49, 5080–5091, 2011.
- Fujisada, H., Urai, M., and Iwasaki, A.: Technical methodology for ASTER global DEM, *IEEE Transactions on Geoscience and Remote Sensing*, 50, 3725–3736, 2012.
- Geng, G., Zhang, Q., Martin, R., Donkelaar, A., Huo, H., CHE, H., Lin, J., and He, H.: Estimating long-term PM_{2.5} concentrations in China using satellite-based aerosol optical depth and a chemical transport model, *Remote Sensing of Environment*, 166, <https://doi.org/10.1016/j.rse.2015.05.016>, 2015.
- 510 Hammer, M. S., van Donkelaar, A., Li, C., Lyapustin, A., Sayer, A. M., Hsu, N. C., Levy, R. C., Garay, M. J., Kalashnikova, O. V., Kahn, R. A., et al.: Global estimates and long-term trends of fine particulate matter concentrations (1998–2018), *Environmental Science & Technology*, 54, 7879–7890, 2020.
- 515 Handschuh, J., Erbertseder, T., and Baier, F.: Systematic Evaluation of Four Satellite AOD Datasets for Estimating PM_{2.5} Using a Random Forest Approach, *Remote Sensing*, 15, <https://doi.org/10.3390/rs15082064>, 2023.
- Health Effects Institute: State of global air 2019, 2019.
- Ibrahim, S., Landa, M., Pešek, O., Brodský, L., and Halounová, L.: Machine Learning-Based Approach Using Open Data to Estimate PM_{2.5} over Europe, *Remote Sensing*, 14, <https://doi.org/10.3390/rs14143392>, 2022.
- 520 Lipponen, A., Kolehmainen, V., Kolmonen, P., Kukkurainen, A., Mielonen, T., Sabater, N., Sogacheva, L., Virtanen, T. H., and Arola, A.: Model-enforced post-process correction of satellite aerosol retrievals, *Atmospheric Measurement Techniques*, 14, 2981–2992, 2021.
- Lipponen, A., Reinval, J., Väisänen, A., Taskinen, H., Lähivaara, T., Sogacheva, L., Kolmonen, P., Lehtinen, K., Arola, A., and Kolehmainen, V.: Deep-learning-based post-process correction of the aerosol parameters in the high-resolution Sentinel-3 Level-2 Synergy product, *Atmospheric Measurement Techniques*, 15, 895–914, 2022.
- 525 Loveland, T. R. and Belward, A.: The international geosphere biosphere programme data and information system global land cover data set (DISCover), *Acta Astronautica*, 41, 681–689, 1997.
- Lundberg, S. M. and Lee, S.: A unified approach to interpreting model predictions, *CoRR*, [abs/1705.07874](https://arxiv.org/abs/1705.07874), <http://arxiv.org/abs/1705.07874>, 2017.
- Michaelides, S., Lane, J., and Kasparis, T.: Effect of Vertical Air Motion on Disdrometer Derived Z-R Coefficients, *Atmosphere*, 10, 77, 530 2019.
- NASA: CALIPSO Data User’s Guide, https://www-calipso.larc.nasa.gov/resources/calipso_users_guide/, [Online; accessed 13-April-2023], 2022.
- NASA/METI/AIST/Japan Spacesystems, and US/Japan ASTER Science Team: ASTER Global Digital Elevation Model V003, distributed by NASA EOSDIS Land Processes DAAC, 2019.
- 535 OpenStreetMap: OpenStreetMap Wiki - Key:highway, <https://wiki.openstreetmap.org/wiki/Key:highway>, [Online; accessed 13-April-2023], 2023.

- Pope, C. A. I. and Dockery, D. W.: Health Effects of Fine Particulate Air Pollution: Lines that Connect, *Journal of the Air & Waste Management Association*, 56, 709–742, <https://doi.org/10.1080/10473289.2006.10464485>, 2006.
- 540 Randles, C., Da Silva, A., Buchard, V., Colarco, P., Darmenov, A., Govindaraju, R., Smirnov, A., Holben, B., Ferrare, R., Hair, J., et al.: The MERRA-2 aerosol reanalysis, 1980 onward. Part I: System description and data assimilation evaluation, *Journal of climate*, 30, 6823–6850, 2017.
- Schneider, R., Vicedo-Cabrera, A. M., Sera, F., Masselot, P., Stafoggia, M., de Hoogh, K., Kloog, I., Reis, S., Vieno, M., and Gasparrini, A.: A Satellite-Based Spatio-Temporal Machine Learning Model to Reconstruct Daily PM_{2.5} Concentrations across Great Britain, *Remote Sensing*, 12, <https://doi.org/10.3390/rs12223803>, 2020.
- 545 Stafoggia, M., Bellander, T., Bucci, S., Davoli, M., de Hoogh, K., de' Donato, F., Gariazzo, C., Lyapustin, A., Michelozzi, P., Renzi, M., Scortichini, M., Shtein, A., Viegli, G., Kloog, I., and Schwartz, J.: Estimation of daily PM₁₀ and PM_{2.5} concentrations in Italy, 2013–2015, using a spatiotemporal land-use random-forest model, *Environment International*, 124, 170–179, <https://doi.org/https://doi.org/10.1016/j.envint.2019.01.016>, 2019.
- Sulla-Menashe, D. and Friedl, M. A.: User guide to collection 6 MODIS land cover (MCD12Q1 and MCD12C1) product, USGS: Reston, VA, USA, 1, 18, 2018.
- 550 Taskinen, H., Väisänen, A., Hatakka, L., Virtanen, T. H., Lähivaara, T., Arola, A., Kolehmainen, V., and Lipponen, A.: High-Resolution Post-Process Corrected Satellite AOD, *Geophysical Research Letters*, 49, e2022GL099733, 2022.
- van Donkelaar, A., Martin, R. V., Spurr, R. J., Drury, E., Remer, L. A., Levy, R. C., and Wang, J.: Optimal estimation for global ground-level fine particulate matter concentrations, *Journal of Geophysical Research: Atmospheres*, 118, 5621–5636, 2013.
- 555 van Donkelaar, A., Martin, R. V., Brauer, M., Hsu, N. C., Kahn, R. A., Levy, R. C., Lyapustin, A., Sayer, A. M., and Winker, D. M.: Global Estimates of Fine Particulate Matter using a Combined Geophysical-Statistical Method with Information from Satellites, Models, and Monitors, *Environmental Science & Technology*, 50, 3762–3772, <https://doi.org/10.1021/acs.est.5b05833>, 2016.
- van Donkelaar, A., Hammer, M. S., Bindle, L., Brauer, M., Brook, J. R., Garay, M. J., Hsu, N. C., Kalashnikova, O. V., Kahn, R. A., Lee, C., Levy, R. C., Lyapustin, A., Sayer, A. M., and Martin, R. V.: Monthly Global Estimates of Fine Particulate Matter and Their Uncertainty, *Environmental Science & Technology*, 55, 15287–15300, <https://doi.org/10.1021/acs.est.1c05309>, 2021.
- 560 Wang, Z., Shrestha, R., and M.O., R.: VIIRS/NPP Lunar BRDF-Adjusted Nighttime Lights Yearly L3 Global 15 arc second Linear Lat Lon Grid [data set], <https://doi.org/10.5067/VIIRS/VNP46A4.001>, 2020.
- Winker, D., Pelon, J., Coakley Jr, J., Ackerman, S., Charlson, R., Colarco, P., Flamant, P., Fu, Q., Hoff, R., Kittaka, C., et al.: The CALIPSO mission: A global 3D view of aerosols and clouds, *Bulletin of the American Meteorological Society*, 91, 1211–1230, 2010.
- 565 World Health Organization: New WHO Global Air Quality Guidelines aim to save millions of lives from air pollution, <https://www.who.int/news/item/22-09-2021-new-who-global-air-quality-guidelines-aim-to-save-millions-of-lives-from-air-pollution>, [Online; accessed 12-April-2023], 2021.
- Zhang, H. and Kondragunta, S.: Daily and Hourly Surface PM_{2.5} Estimation From Satellite AOD, *Earth and Space Science*, 8, e2020EA001599, <https://doi.org/https://doi.org/10.1029/2020EA001599>, e2020EA001599 2020EA001599, 2021.